



Research on Microstructure, Mechanical Properties and Electromagnetic Shielding Properties of Mg-6Zn-3Sn-0.5Cu Alloy

Yan Hui Liu^{1,2,3}, Ming Long Ma^{1,2,3*}, Xing Gang Li^{1,2,3}, Yong Jun Li^{1,2,3}, Guo Liang Shi^{1,2,3}, Jia Wei Yuan^{1,2,3} and Kui Zhang^{1,2,3*}

¹State Key Laboratory of Nonferrous Metals and Processes, GRINM Co., Ltd., Beijing, China, ²GRIMAT Engineering Institute Co., Ltd., Beijing, China, ³General Research Institute for Nonferrous Metals, Beijing, China

OPEN ACCESS

Edited by:

Lai-Chang Zhang,
Edith Cowan University, Australia

Reviewed by:

Xiaodong Peng,
Chongqing University, China
Bo Song,
Southwest University, China
Xianhua Chen,
Chongqing University, China

*Correspondence:

Ming Long Ma
maminglong@grinm.com
Kui Zhang
zhkui@grinm.com

Specialty section:

This article was submitted to
Structural Materials,
a section of the journal
Frontiers in Materials

Received: 17 September 2021

Accepted: 20 October 2021

Published: 03 November 2021

Citation:

Liu YH, Ma ML, Li XG, Li YJ, Shi GL,
Yuan JW and Zhang K (2021)
Research on Microstructure,
Mechanical Properties and
Electromagnetic Shielding Properties
of Mg-6Zn-3Sn-0.5Cu Alloy.
Front. Mater. 8:778833.
doi: 10.3389/fmats.2021.778833

In this paper, the microstructure, electromagnetic shielding properties and mechanical properties of Mg-6Zn-3Sn-0.5Cu alloys are studied. As indicated from the results, the phases in the as-cast alloy comprise α -Mg, MgZnCu, Mg₂Sn and Mg₂Zn₃ phases. After homogenization, Mg₂Sn and Mg₂Zn₃ phases are decomposed, but the MgZnCu phase remains. During extrusion, complete dynamic recrystallization (DRX) occurs, and the spherical Mg₂Sn phase precipitates dynamically. Due to considerable rod-like β'_1 phases precipitate by complying with the [0001]_{Mg} direction, the mechanical properties of aged alloys are remarkably enhanced. The peak-aged alloy achieves the tensile strength of 366 MPa, the yield strength of 358 MPa and the elongation of 7%. With the increase in the size of the β'_1 phase, the mechanical properties of the over-aged alloy are reduced. Since the phases precipitate, the electrical conductivity of the alloy is enhanced, and the internal reflective interface increases, so the aged alloys exhibit improved electromagnetic shielding performance. The electromagnetic shielding efficiency of the peak-aged alloy exceeds 105 dB in the range of 30–1500 MHz, showing the best match between mechanical and electromagnetic shielding properties.

Keywords: Mg-Zn-Sn-Cu alloy, extrusion, aging treatment, mechanical properties, electromagnetic shielding properties

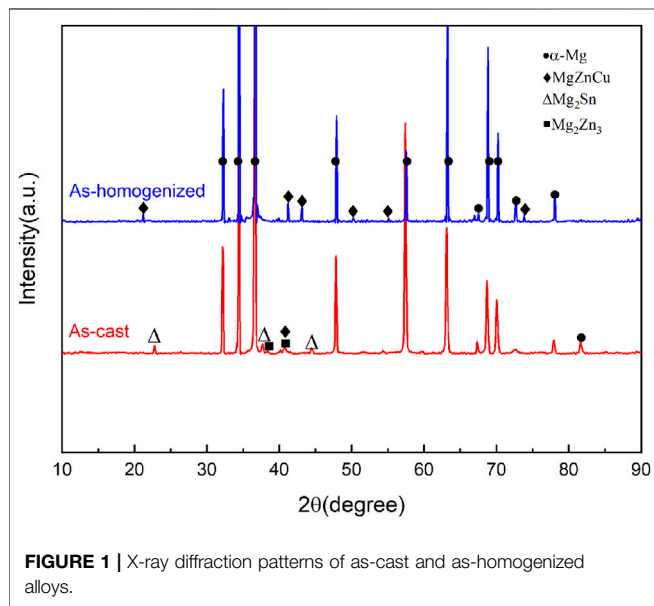
INTRODUCTION

As modern electronic technology is advancing, people's production life has been facilitated, while the issue of electromagnetic pollution has arisen. Electromagnetic waves are capable of affecting the life and health of living organisms and interfering with the normal operation of electronic equipment. Moreover, the risk of information leakage in national defense will be raised if electromagnetic waves are not effectively shielded (García et al., 2008; Shen et al., 2013; Shahzad et al., 2016; Kim et al., 2017). On the whole, the existing electromagnetic shielding materials complies with polymer composites and metal-based materials, whereas polymer materials exhibit poor mechanical properties, and metal-based materials face a problem of high density (Geetha et al., 2009). For this reason, the development of lightweight electromagnetic shielding materials with high mechanical properties has become one of the hotspots in materials research.

Magnesium alloys have been extensively employed in automotive, aerospace, defense and military industries for their low density, high specific strength over stiffness, good damping properties and

TABLE 1 | Chemical composition of the experimental alloy (wt.%).

Alloy	Nominal compositions	Actual compositions			
		Zn	Sn	Cu	Mg
ZT63-0.5Cu	Mg-6Zn-3Sn-0.5Cu	5.8	3.38	0.48	Bal.



easy recycling (Ali et al., 2015; You et al., 2017). At present, in addition to studying the microstructure and mechanical properties of magnesium alloys, the study of their functional properties has also become an emerging research hotspot (Yang et al., 2021). Electromagnetic shielding performance as an important functional property of magnesium alloys has also attracted the attention of researchers. Pandey et al. (2019) found that the addition of Ti can improve the electromagnetic shielding performance of pure magnesium. Wang et al. (2019) developed an Mg-Li alloy with high mechanical and electromagnetic shielding properties by rolling. Ye et al. (2021) prepared an Mg-Sn-Zn alloy with a tensile strength of 337 MPa and an electromagnetic shielding efficiency of 97–114 dB, which had a good comprehensive performance. Chen et al. (2012), Chen et al. (2013), and Chen et al. (2015a) revealed that aging treatment could improve the electromagnetic shielding properties of Mg-Zn alloys. By introducing suitable alloying elements to the alloy, combined with plastic deformation and aging treatment, magnesium alloys with high electromagnetic shielding properties and prominent mechanical properties can be prepared, which is critical to expanding the application of magnesium alloys.

Mg-Zn alloys can be strengthened by heat treatment, and their cost is significantly lowered compared with rare-earth magnesium alloys. However, the mechanical properties of Mg-Zn alloys are poor, and further alloying is required to enhance the properties of the alloys. For example, elements such as Sn, Ca,

Mn, and Cu are added to the Mg-Zn alloys to improve their mechanical properties (Liu et al., 2020; Wang et al., 2021). As reported by Wei et al. (2013) and Qi et al. (2014), the addition of Sn elements to Mg-Zn alloys resulted in grain refinement and improvement of mechanical properties. Wang et al. (2018) reported that the Cu element could refine the second phase in Mg-Sn-Zn alloy and enhance the mechanical properties of the alloy.

As indicated from recent studies, Mg-Zn alloys also exhibit high electromagnetic shielding properties (Chen et al., 2012; Chen et al., 2013; Chen et al., 2015a). However, research on structural-functional integration Mg-Zn alloys is still relatively rare. Rare research has been reported on. Thus, to further expand the application of Mg-Zn alloy and enrich its basic theoretical data as structural-functional materials, we prepared Mg-6Zn-3Sn-0.5Cu alloy based on Mg-6Zn-3Sn alloy with the addition of a trace amount of Cu elements. The microstructure evolution of the alloy was studied, and the mechanical properties and electromagnetic shielding properties of the extruded, peak-aged and over-aged alloy were analyzed. Such a study will provide novel ideas for preparing low-cost and high-performance magnesium alloys.

MATERIALS AND METHODS

The raw materials applied for preparing the alloy included pure Mg (99.95%), pure Zn (99.95%), pure Sn (99.99%) and pure Cu (99.99%), which were melted in a medium frequency induction furnace. A mixture of argon and tetrafluoroethane (Ar: CH₂FCF₃ = 20:1) was introduced in the melting to protect the melt, the final size of the ingot reached $\Phi 100 \times 360$ mm. The element content of the ingots was determined with Inductively Coupled Plasma-Atomic Emission Spectrometry (ICP-AES), and the results are listed in **Table 1**. The ingots were homogenized at 335°C–24h + 420°C–24h and then extruded at 370°C at an extrusion speed of 0.6 mm/s as well as an extrusion ratio of 23:1. The final extruded bar with a diameter of 25 mm was obtained. The alloy was aged at 180°C under an aging period of 0–100 h.

The microstructure of the alloy was explored under an optical microscope (OM, Carl Zeiss Axiovert2000MAT), a field emission scanning electron microscope (FE-SEM, JEOL JSM-7600), an X-ray diffractometer (XRD, Smartlab), as well as a transmission electron microscope (TEM, Tecnai G2 F20). JEOL JSM-7900F equipped with an electron backscattered diffraction (EBSD) system was used to analyze the texture of the alloy. The etchant for the alloy is a mixture of ethanol (10 ml) + picric acid (0.3 g) + glacial acetic acid (1 ml) + distilled water (1 ml). EBSD samples were electropolished in a 10% nitric acid alcohol solution. The average grain size of the alloy was determined by the linear intercept method. The tensile properties for the different state alloy were obtained by a SANS universal testing machine. Cylindrical samples of diameter 5 mm and gauge length 25 mm were used for tensile tests. Three tensile tests were

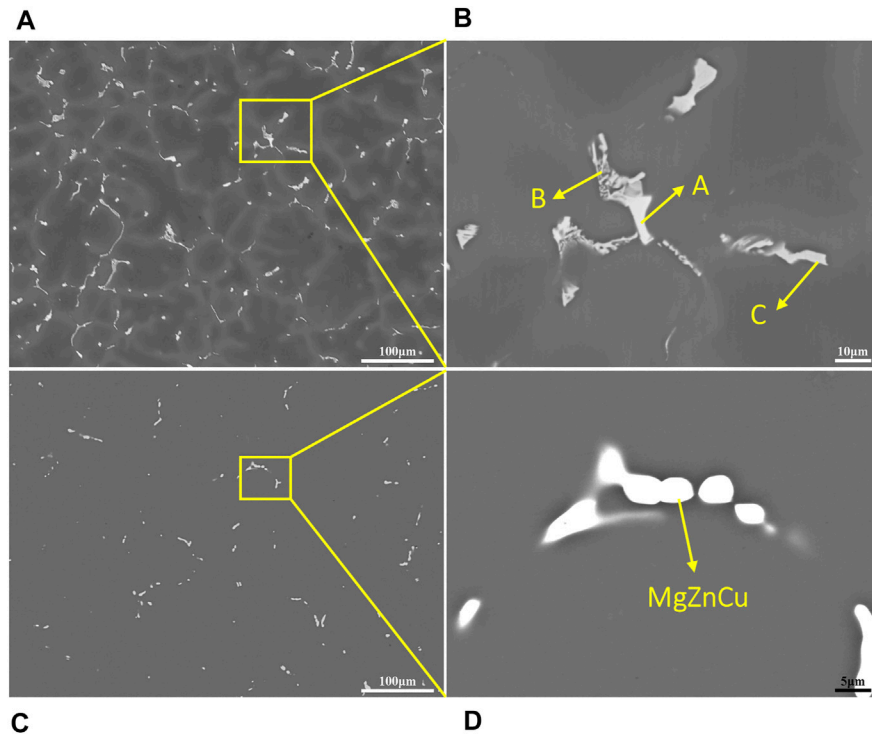


FIGURE 2 | SEM images of as-cast and as-homogenized alloys: (A,B) as-cast alloy, (C,D) as-homogenized alloy.

TABLE 2 | EDS results for different positions of as-cast alloy.

Point	Mg		Sn		Zn		Cu	
	At. %	Wt. %						
A	72.32	35.47	26.05	62.39	1.24	1.64	0.39	0.50
B	70.76	47.32	0.32	1.03	21.94	39.46	6.98	12.19
C	64.99	40.21	1.13	3.41	33.88	56.38	—	—

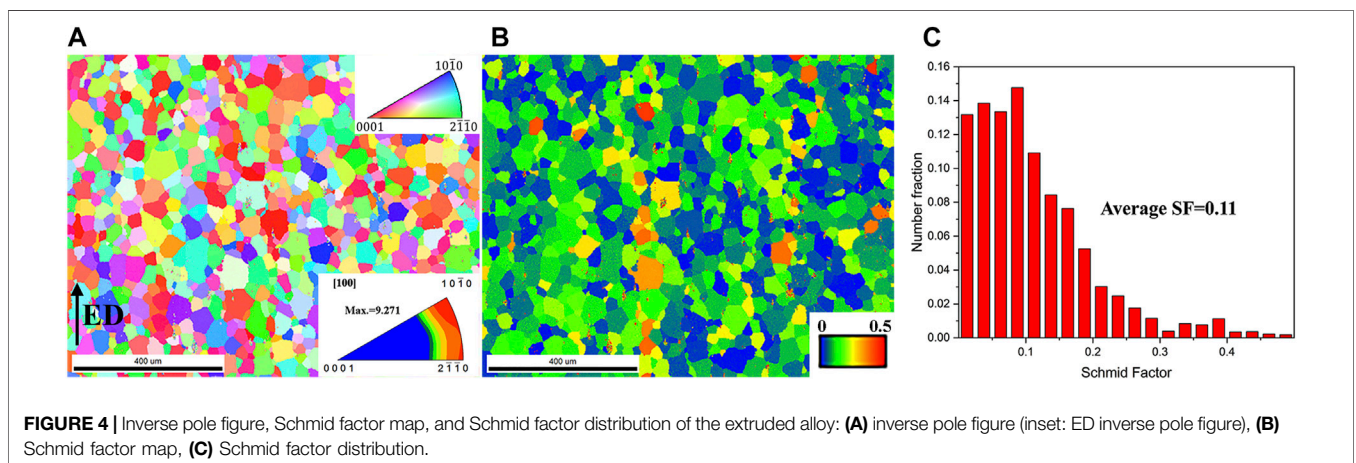
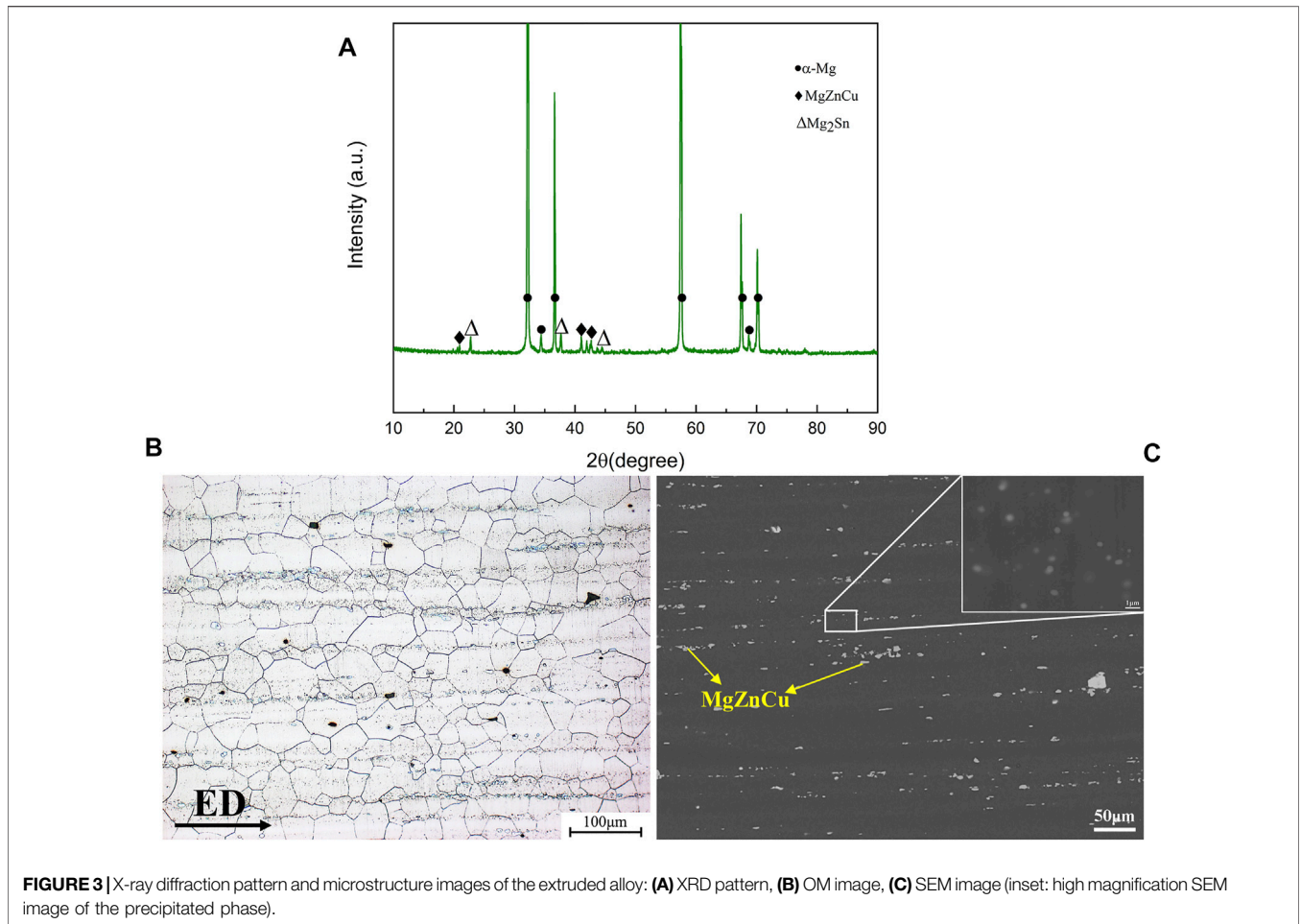
performed, and the strength and elongation were taken as the mean value. A Brinell hardness tester (HBS 62.5) was employed to examine the hardness of the alloy during aging. The load during the test was 30 kg and the loading time was 25 s. Each sample was tested five times, and the average hardness value was taken. The electrical conductivity of the alloy was tested with a WD-Z eddy current conductivity tester, with the respective sample being tested five times, and the final result was taken as the mean value. The standard coaxial cable method was employed to measure the electromagnetic shielding properties of the different state alloys. The electromagnetic shielding test equipment involved an E6063A vector network analyzer and a DR-S04 micro-coaxial shield effectiveness tester. The samples were taken from the cross-section of the bar, with a diameter of 20 mm and a thickness of 0.9 mm. The electromagnetic wave frequency range of the test was 30–1500 MHz. Each sample was tested five times, and the final shielding effectiveness was taken as its average value.

RESULTS AND DISCUSSION

Microstructure of As-Cast and As-Homogenized Alloys

The XRD patterns of the as-cast and as-homogenized alloys are illustrated in **Figure 1**. α -Mg, MgZnCu phase, Mg₂Sn phase and Mg₂Zn₃ phase are found in the as-cast alloy. After the homogenization treatment, the diffraction peaks belonging to the Mg₂Sn and Mg₂Zn₃ phases disappear, and only the diffraction peak of the MgZnCu phase existed except for the α -Mg, which demonstrates that the homogenization can make the Mg₂Sn and Mg₂Zn₃ phases decompose, and the Zn and Sn atoms dissolve back into the matrix, while the MgZnCu phase is not decomposed.

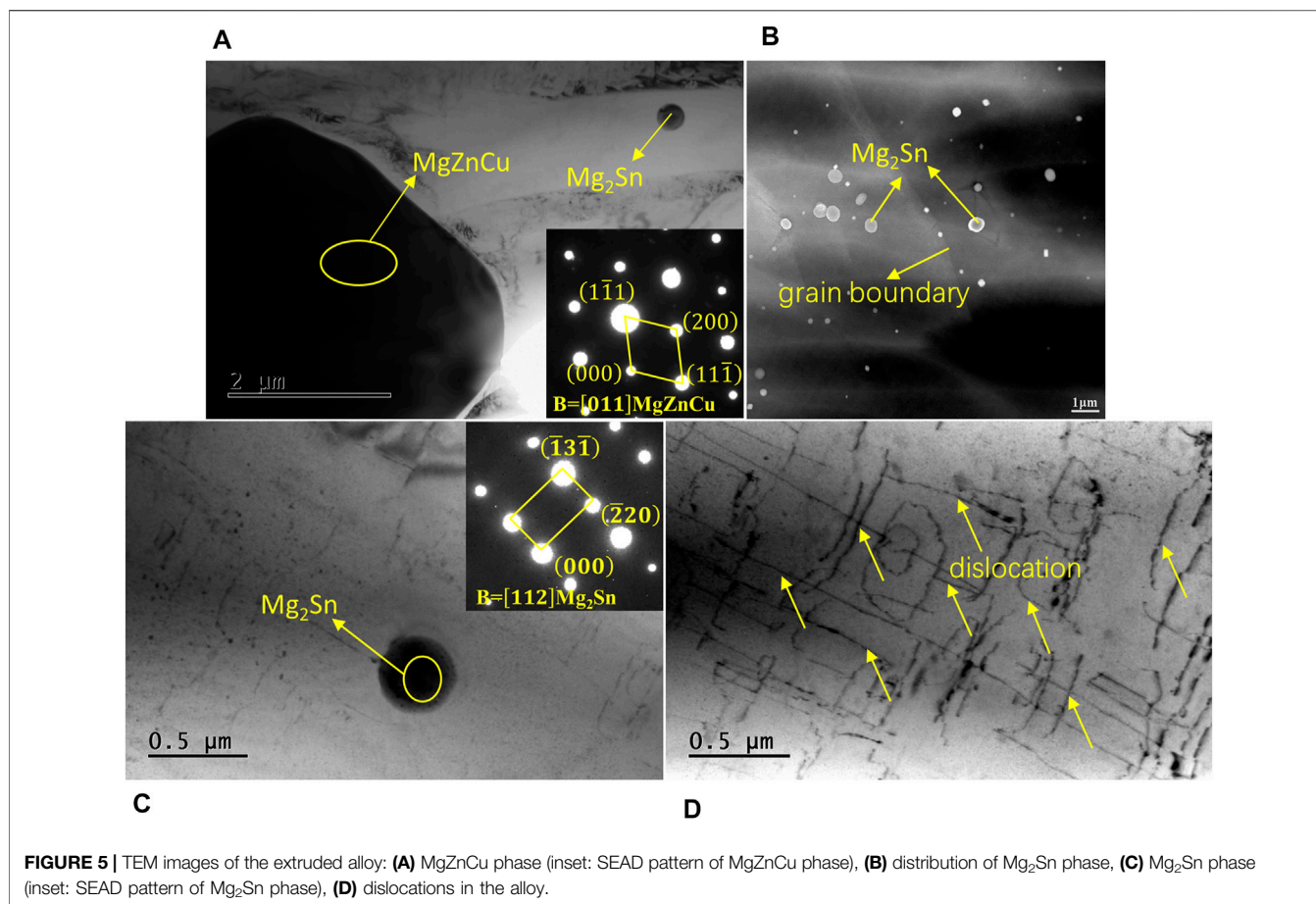
Figure 2 presents the SEM images of the as-cast and as-homogenized alloys. As indicated from the low magnification SEM image (**Figure 2A**), the as-cast alloy displays a typical petal-like dendritic structure, with the eutectic compounds primarily distributed on the grain boundaries. As suggested from the high magnification SEM image (**Figure 2B**), the eutectic compounds are mainly skeletal and massive in shape. The results of the EDS composition analysis of the eutectic compounds at different locations (marked as A, B, and C in **Figure 2B**) are listed in **Table 2**. Given the EDS and XRD results, the skeletal phase is the MgZnCu phase and the bulk phase refers to the Mg₂Sn phase or Mg₂Zn₃ phase. **Figure 2C** shows that the dendritic morphology of the alloy disappears after homogenization, the segregation of elements at the grain boundaries is noticeably reduced and the



eutectic compounds are largely decomposed, but some of the granular or lumpy phases remain at the grain boundaries. Given the XRD results, the residual second phase is the MgZnCu phase (Figure 2D), which is a thermally stable phase that fails to decompose during homogenization.

Microstructure of the Extruded Alloy

Figure 3 presents the XRD pattern, OM and SEM images of the extruded alloy. XRD pattern reveals that the Mg₂Sn phase appears in the extruded alloy besides the MgZnCu phase and the α-Mg, thereby indicating that the dynamic precipitation of the Mg₂Sn



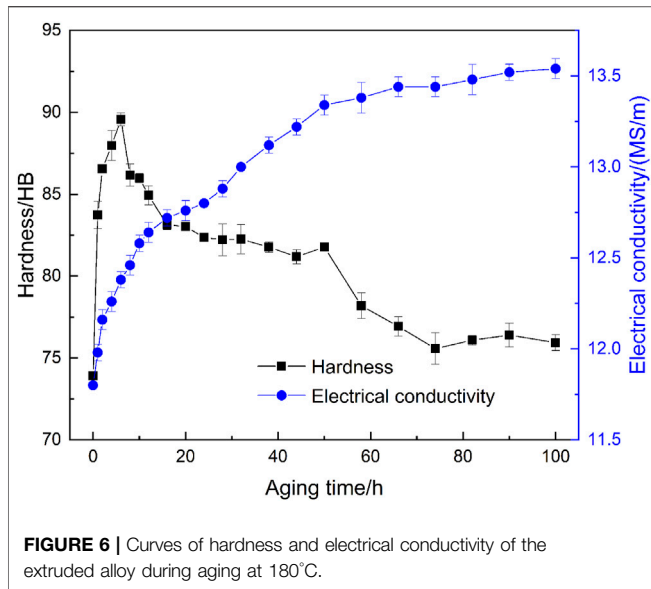
phase occurs in the extrusion (**Figure 3A**). **Figure 3B** shows that complete dynamic recrystallization (DRX) takes place in the extrusion, and the dynamically recrystallized grains are equiaxed with an average size of approximately 39 μm . As indicated in **Figure 3C**, besides the broken MgZnCu phase, there are also numerous dispersed spot phases in the alloy. Combined with the XRD results, it can be concluded that the phase is the Mg₂Sn phase.

For the extruded alloy, texture also affects its properties. The inverse pole figure of the extruded alloy (**Figure 4A**) reveals that it exhibits a basal fiber texture, in which the (0001) plane is preferentially parallel to the extrusion direction (ED). The texture type is $\langle 10\text{-}10 \rangle // \text{ED}$, $\langle 2\text{-}1\text{-}10 \rangle // \text{ED}$ and the maximum intensity is 9.271. Schmid factor (SF) map and Schmid factor distribution for the basal slip system of the alloy indicate that the alloy has a low SF value of 0.11 (**Figure 4B**). The low Schmid factor means that basal slip is difficult to activate, enabling the alloy to exhibit a high yield strength.

TEM images of the extruded alloy are presented in **Figure 5**. The larger phase can be identified as the MgZnCu phase (**Figure 5A**). **Figure 5B** indicates that the dynamically precipitated Mg₂Sn phase is spherical, distributed near the grain boundaries, with sizes ranging from 200–500 nm. SEAD pattern of the phase reveals it has a face-centered cubic structure

(FCC, $a = 0.6763 \text{ nm}$) (**Figure 5C**). Moreover, a certain number of dislocations in the alloy are observed in the TEM bright-field image (**Figure 5D**).

The precipitation of the Mg₂Sn phase is closely related to the deformation temperature and the stress state during the deformation process. The eutectic temperature of Mg-Sn is 567°C, and the solid solubility of Sn increases with the rise of the temperature (Ghosh et al., 2012). With the deformation temperature lower than the homogenization temperature, the Mg₂Sn phase exerts a certain precipitation driving force. In addition, the compressive stress in the extrusion process also facilitates the precipitation of the Mg₂Sn phase (Kabir et al., 2014). Accordingly, under the combined effect of temperature and stress, the Mg₂Sn phase with a high eutectic temperature can precipitate from the matrix. The statically precipitated Mg₂Sn phase has a range of forms, whereas the dynamically precipitated Mg₂Sn phase during extrusion is subjected to stress, thereby leading to its spherical precipitation. In addition, it has been shown that Zn elements can reduce the activation energy of the Mg₂Sn phase nucleation by reducing the interfacial energy at the Mg₂Sn-Mg interface, thus promoting the precipitation of the Mg₂Sn phase (Sasaki et al., 2011; Liu et al., 2016). Zn elements solid dissolved in the matrix during homogenization undoubtedly facilitate the precipitation of the Mg₂Sn phase. The precipitated Mg₂Sn, in turn, hinders the growth of recrystallized grains (Sasaki



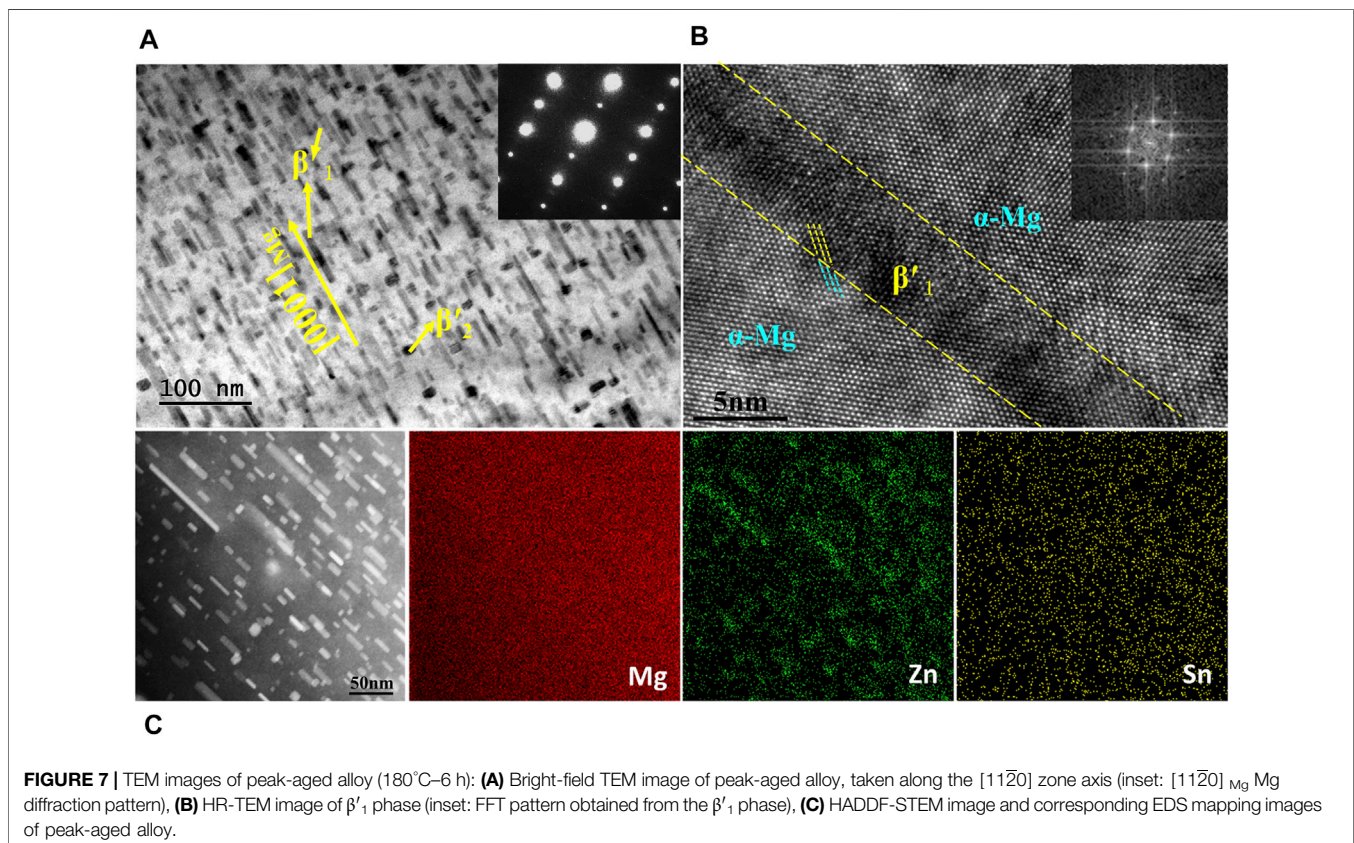
et al., 2008), thereby improving the mechanical properties of the alloy.

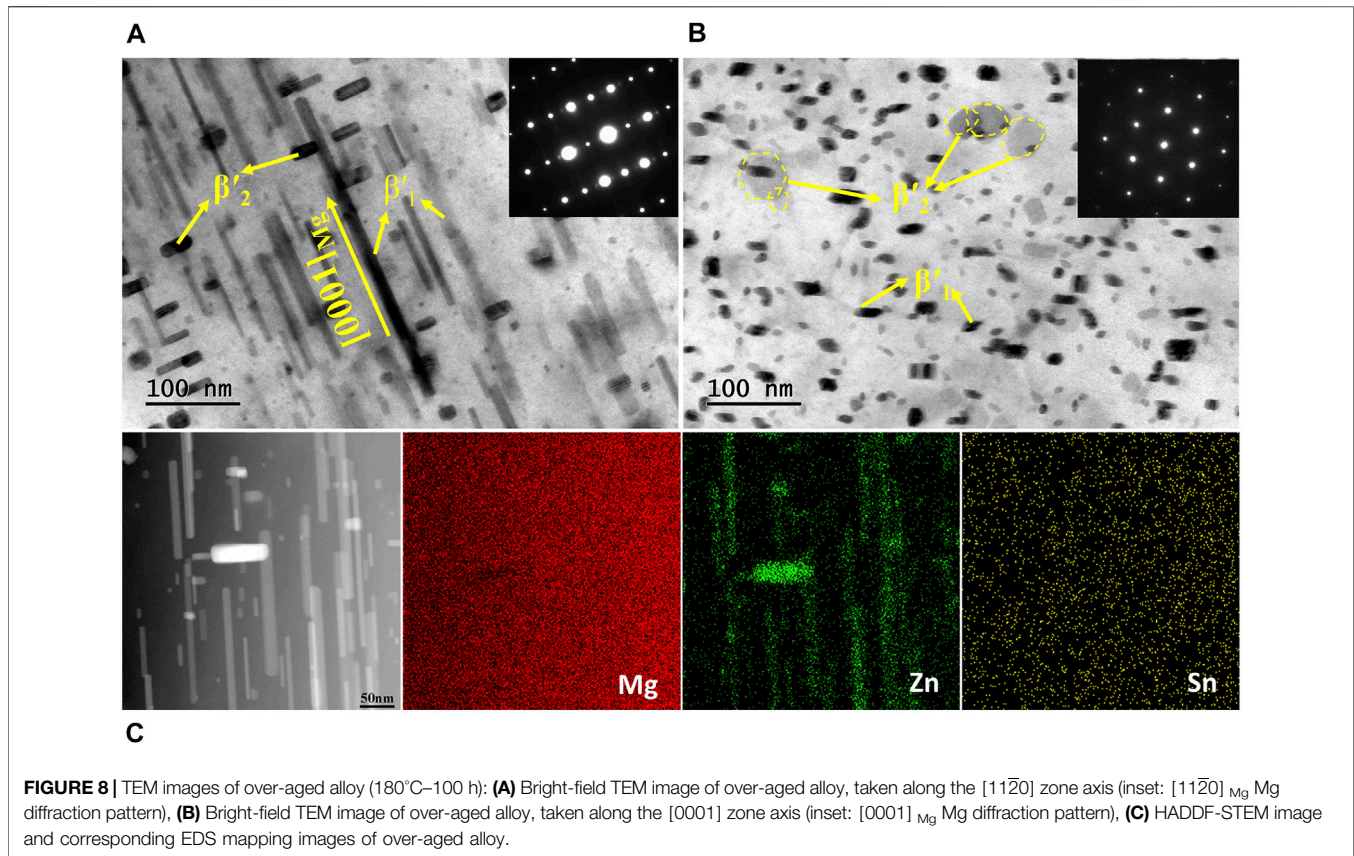
Microstructure of the Aged Alloy

Figure 6 presents the changes in hardness and electrical conductivity of the extruded alloy during aging at 180°C. The

hardness of the alloy increases rapidly first and then decreases with time, reaching a peak at 6 h. Compared with the extruded alloy, the hardness of the peak-aged alloy increases significantly, which demonstrates a strong aging strengthening effect. At the early stage of aging, the second phase gradually precipitates, and the phase density increases. The denser the phase is distributed, the stronger its resistance to dislocation motion (Kim and Park, 2016). Therefore, the hardness of the alloy continues to increase until reaches its peak. With the extension of time, the size of the precipitated phase increases, leading to a decrease in dislocation hindrance efficiency and a drop in hardness. In addition, the electrical conductivity of the alloy rises continuously over time. This is because the scattering effect of the second phase on the electrons is significantly weaker than that of the solid solution atoms (Pan et al., 2013). As the second phase continues to precipitate, the content of solute solution atoms in the matrix is reduced, the lattice distortion of the matrix declines, the chance of being scattered during electron transport is lowered, and the conductivity of the alloy increases continuously.

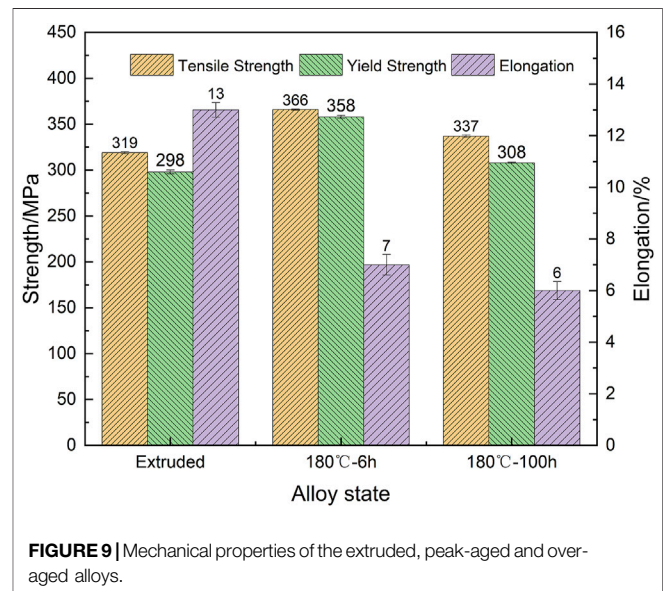
Figure 7 gives TEM images of the peak-aged alloy. Considerable rod-shaped phases precipitate in the alloy, complying with the long axis of $[0001]_{\text{Mg}}$ and ranging from 10 to 20 nm in the size (**Figure 7A**). Based on their morphology and orientation as well as high-resolution TEM image, they are identified as β'_1 precipitates (Rashkova et al., 2008; Ren et al., 2021). They stand for the main strengthening precipitates in Mg-Zn alloys (Rosalie and Pauw, 2014; Alizadeh et al., 2021). The





high-resolution TEM image of the β'_1 phase in **Figure 7B** indicates that the β'_1 phase is fully coherent with the α -Mg matrix. The precipitates in this coherent relationship with the matrix are more effective in impeding the movement of dislocations, increasing the hardness, and improving the mechanical properties of the alloy. Besides the densely distributed β'_1 phase, there are also precipitated phases perpendicular to the β'_1 phase in orientation. They are identified as the β'_2 phase, which are distributed on the basal plane (0001) of α -Mg (Ren et al., 2021). According to **Figure 7C**, only Mg-Zn phases precipitate during aging, and no precipitation of the Mg-Sn phase is observed.

Figure 8 illustrates the TEM images of the over-aged alloy. Both the β'_1 and β'_2 phases grow significantly with the prolonging of the aging time, and the β'_1 phase is converted into a slender rod shape (**Figure 8A**). Moreover, the β'_2 phase is observed to be disk-shaped from the $[0001]_{\text{Mg}}$ direction (**Figure 8B**), which has a lower amount compared with the β'_1 phase. It is noteworthy that the precipitation of the Mg-Zn phase is predominant in the aging process, and no precipitation of the Mg-Sn phase is observed even with the aging time extended to 100 h (**Figure 8C**). This phenomenon may be explained as the dynamic precipitation of the Mg_2Sn phase in the extrusion consumes considerable Sn elements, and the low Sn content in the matrix, together with the low aging temperature, results in a lack of motivation for the precipitation of the Mg-Sn phase.



Mechanical Properties of the Alloys

The room temperature tensile mechanical properties of the extruded, peak-aged and over-aged alloys are illustrated in **Figure 9**. The tensile strength, yield strength and elongation of the extruded alloy reach 319 MPa, 298 MPa and 13%,

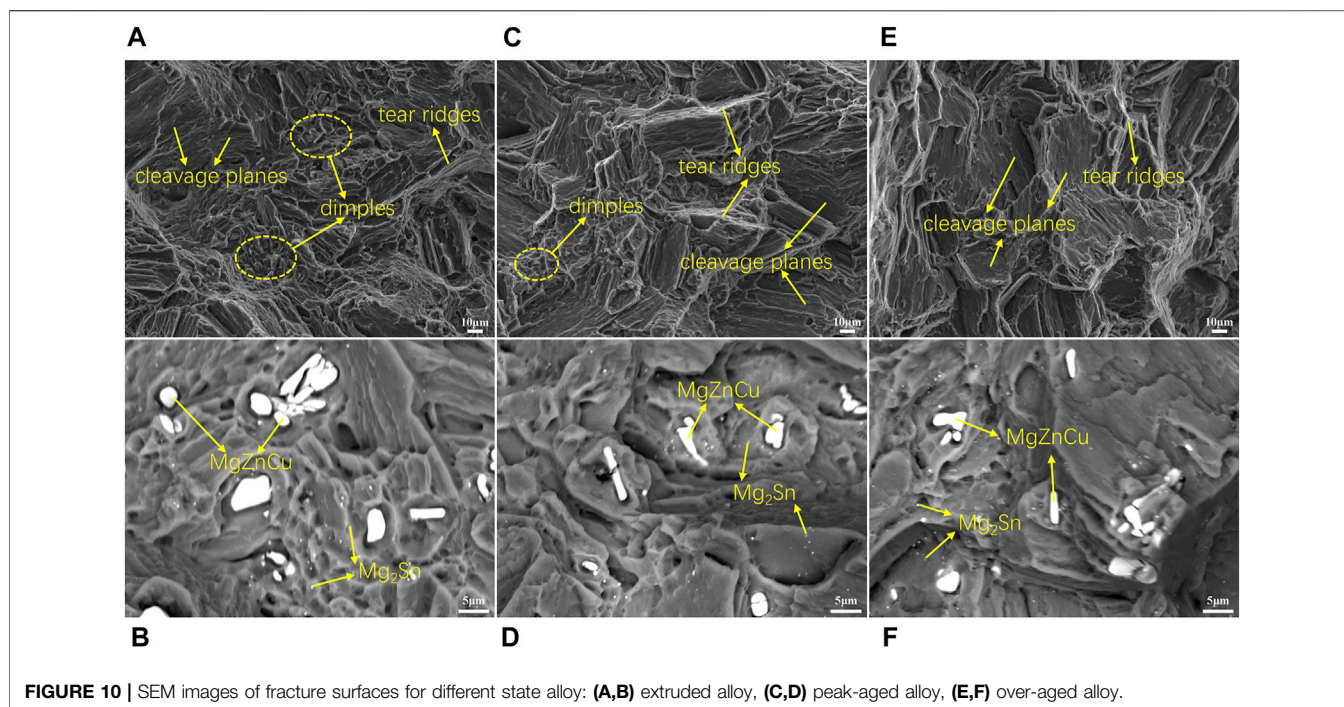


FIGURE 10 | SEM images of fracture surfaces for different state alloy: **(A,B)** extruded alloy, **(C,D)** peak-aged alloy, **(E,F)** over-aged alloy.

respectively. The tensile and yield strengths of the peak-aged alloy substantially increase compared with the extruded alloy, with the tensile strength increasing by 47 MPa and the yield strength by 60 MPa, whereas the elongation is reduced to only 7%. In comparison with the peak-aged alloy, the mechanical properties of the over-aged alloy are reduced, to be specific, the tensile strength is reduced to 337 MPa, the yield strength declines to 308 MPa, and the elongation is approximately 6%.

Many factors are affecting the mechanical properties of the alloy. For the extruded alloy, complete dynamic recrystallization takes place, forming recrystallized grain structure, which can be the basis for high mechanical properties. Secondly, considerable Zn atoms are solid dissolved in the extruded alloy. The solid dissolved Zn atoms interact with dislocation, hindering dislocation movement and improving the mechanical properties of the alloy. In addition, the size of the Mg_2Sn phase precipitated during extrusion ranges from 200 to 500 nm, thereby exerting a small effect on dislocation, whereas it can hinder the sliding of grain boundaries and thus improve the mechanical properties of the alloy. Lastly, the extruded alloy develops a strong fiber texture with the basal plane (0001)//ED. When the alloy is deformed under the tensile stress in the ED, the Schmid factor (SF) along the basal plane equaled to 0, and the basal slip is difficult to activate, thereby improving the yield strength of the alloy (Chen et al., 2005; Wu et al., 2020; Li et al., 2021). In general, the high mechanical properties of the extruded alloy are attributed to the combined strengthening mechanisms (e.g., grain refinement, solid solution strengthening, precipitation strengthening, as well as texture strengthening). For the peak-aged alloys, the fine and dense short rod-like β'_1 phase precipitates along with the [0001]_{Mg} orientation, completely coherent with the matrix, and a large coherent strain field is generated, thereby interacting with dislocations and hindering dislocation slip. On that basis, the mechanical properties of the peak-

aged alloy are improved. As the aging process continues, the size of the β'_1 phase increases, the number of the β'_1 phase is lowered, and the corresponding strengthening effect weakens. Therefore, the mechanical properties of the over-aged alloy decrease. In general, the precipitation strengthening effect of β'_1 phases is the main reason for the improved mechanical properties of the peak-aged alloy.

To analyze the fracture mode of the extruded, peak-aged and over-aged alloys, SEM images of fracture surfaces for these alloys are illustrated in **Figure 10**. There are a certain amount of dimples in the fracture surface of the extruded alloy; moreover, part of the cleavage planes and tearing ridges are founded, so a ductile-brittle mixed fracture mode is presented (**Figure 10A**). The number of dimples in the peak-aged alloy (**Figure 10C**) decreases significantly compared with that of extruded alloy, and the cleavage plane rises, which demonstrates that the plasticity of the alloy decreases, as reflected in a decrease in the elongation. The smooth cleavage plane in the over-aged alloy (**Figure 10E**) further increases, and dimples are hardly visible, which demonstrates that the fracture mechanism of the over-aged alloy is characterized by the brittle fracture mode. In addition, as indicated from the high-magnification BEI images of fracture surfaces for the extruded, peak-aged and over-aged alloys (**Figures 10B,D,F**), some MgZnCu phases are distributed at the bottom of dimples, and the MgZnCu phases are partially broken. In addition, precipitated Mg_2Sn phase during extrusion is also observed, mainly distributed near the dimple. The MgZnCu phase is brittle (Cheng et al., 2014), its presence accounts for the fracture failure of the alloy. When the alloy is subjected to external forces, stress concentration will occur near the MgZnCu phase, and MgZnCu particles can be the nucleation sites of microcracks formed by a void nucleation and coalescence mechanism (Zhu et al., 2011), eventually leading to the fracture failure of the alloy.

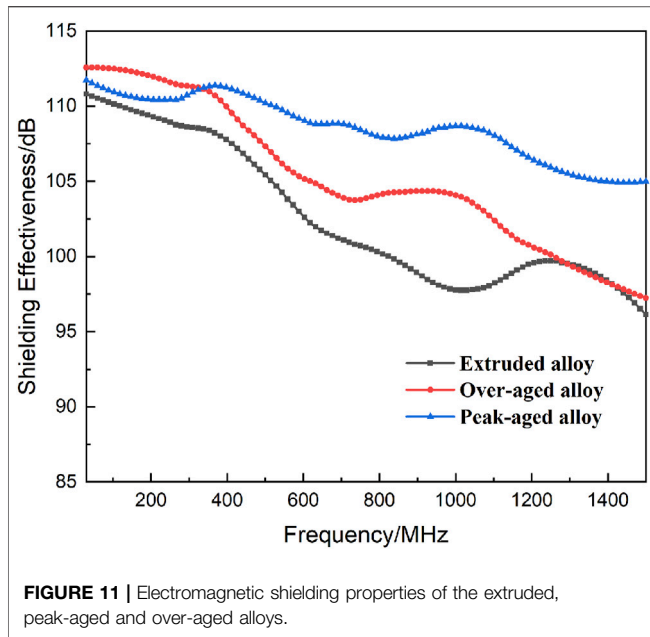


FIGURE 11 | Electromagnetic shielding properties of the extruded, peak-aged and over-aged alloys.

Electromagnetic Shielding of the Alloys

Figure 11 presents the frequency dependence of EMI shielding performance of the extruded, peak-aged and over-aged alloys. In the frequency range of 30–1500 MHz, the electromagnetic shielding effectiveness of the alloys gradually decreases with the increase in the electromagnetic wave frequency. The shielding efficiency of the extruded alloy exceeds 95 dB throughout the whole range, while the peak-aged alloy exhibits a significantly higher shielding efficiency than the extruded alloy, higher than 105 dB throughout the range. Moreover, the over-aged alloy exhibits a lower shielding performance compared with the peak-aged alloy, with a shielding efficiency between 97 and 112 dB, which can still be better than that of the extruded alloy. The peak-aged alloy exhibits the optimal electromagnetic shielding performance. **Table 3** gives a comparison of tensile strengths and SE results of the studied alloy with other alloys in the literature. Obviously, the alloys obtained in this paper have excellent comprehensive performance.

According to the transmission line theory, the attenuation of electromagnetic waves by a shield is achieved by three mechanisms, i.e., reflection attenuation, absorption attenuation and multiple reflection attenuation. The electromagnetic shielding efficiency can be calculated by the following equations (Schulz et al., 1988; Tong, 2009).

$$SE = SE_A + SE_R + SE_M \quad (1)$$

$$SE_A = 131.43t \sqrt{f\mu_r\sigma_r} \quad (2)$$

$$SE_R = 168.2 + 10 \lg[\sigma_r / (f\mu_r)] \quad (3)$$

$$SE_M = 20 \lg(1 - e^{-2t/\delta}) \quad (4)$$

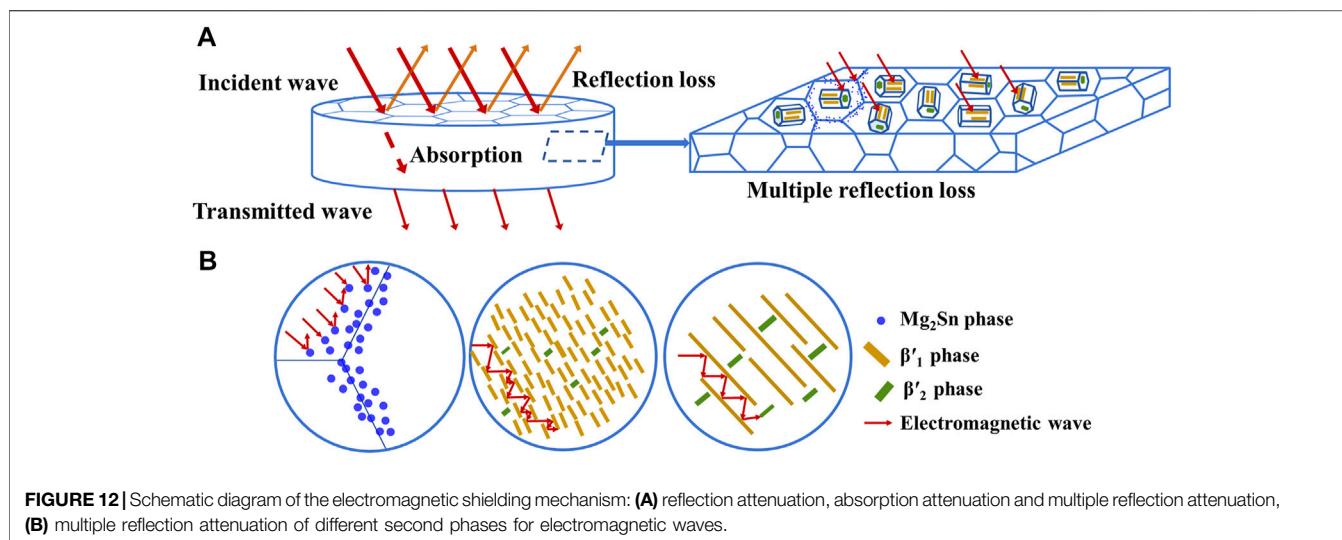
where A denotes the absorption attenuation; R represents the reflection attenuation; M expresses the multiple reflection attenuation; t is the thickness of the material (m); f denotes the

TABLE 3 | Comparison of tensile strengths and SE results between the studied alloys and alloys in the literature.

Alloys	Tensile strength/MPa	SE/dB	References
Extruded alloy	319	96–110	This work
Peak-aged alloy	366	106–111	
Over-aged alloy	337	97–112	
ZK50-2.5Cu	306	84–118	Chen et al. (2015b)
ZK60	~300	65–85	Chen et al. (2013)
Mg-9Li-3Al-1Zn	241	98–107	Wang et al. (2020)

electromagnetic wave frequency (Hz); μ_r and σ_r are relative magnetic permeability and electrical conductivity relative to copper, respectively; δ expresses the skin depth of the material, $\delta = \sqrt{1/\pi\mu\sigma f}$, with μ and σ as the intrinsic magnetic permeability and electrical conductivity of the material, respectively. As indicated from the equations, the electromagnetic shielding performance of the alloy is significantly impacted by its electrical conductivity. A schematic diagram of the electromagnetic shielding mechanism of the alloy is shown in **Figure 12A**. In addition, it has also been shown that the presence of a large number of second phases will enhance the multiple reflection attenuation and improve the electromagnetic shielding properties of the alloy (Chen et al., 2015b).

The electrical conductivity for the extruded, peak-aged and over-aged alloy are 11.7 Ms/m, 12.4 Ms/m, 13.5 Ms/m, respectively. Notably, the conductivity of the alloy increases after aging treatment, whereas the electromagnetic shielding performance exhibited by the alloy fails to increase monotonically with the increase in conductivity. Thus, electrical conductivity can not be a single factor affecting the electromagnetic shielding performance of the alloy, and the transmission line theory has certain limitations. The effect of the fine structure of the alloy on its electromagnetic shielding performance should be further considered. In general, the conductivity of the precipitated phase is significantly lower than that of the matrix, and there is a serious impedance mismatch at the interface between the precipitated phase and the matrix. Thus, electromagnetic waves will be reflected when reaching the phase interface. Accordingly, the precipitation of Mg_2Sn , β'_1 and β'_2 phases will remarkably increase the phase interface in the alloy, and the multiple reflections of electromagnetic waves will be noticeably enhanced as they advance in the alloy, thereby improving the electromagnetic shielding performance of the alloy (Chen et al., 2015a; Wang et al., 2020). The diagram of the multiple reflections of electromagnetic waves for different second phases is presented in **Figure 12B**. As obviously indicated from the figure, the precipitation of the dense β'_1 phase in the peak-aged alloy results in a significant increase in the proportion of phase interface area in the alloy, thereby endowing the alloy with excellent electromagnetic shielding properties. After the aging period is extended to 100h, the electromagnetic shielding performance of the over-aged alloy decreases compared with the peak-aged alloy, which demonstrates that the size of the precipitated phase also impacts the electromagnetic shielding performance of the alloy. As illustrated in **Figure 12B**, the size of the β'_1 phase increases significantly in the over-aged alloy. The phase interface in the over-aged alloy is significantly reduced compared with the peak-aged alloy, and the multiple reflection attenuation of the precipitated phase on the



electromagnetic waves is correspondingly weakened (Chen et al., 2013), so the electromagnetic shielding performance of the over-aged alloy decreased. The factors influencing the electromagnetic shielding performance of the alloy are complex, whereas it can be generally conducive to obtaining the alloy exhibiting high electromagnetic shielding properties through appropriate alloy composition design combined with deformation and heat treatment means to endow the alloy with higher electrical conductivity and more reflective interfaces.

CONCLUSION

The microstructure, mechanical properties and electromagnetic shielding properties exhibited by Mg-6Zn-3Sn-0.5Cu alloy are explored, and possible shielding mechanisms and strengthening mechanisms are analyzed. The conclusions are drawn below:

- 1) The phases in the as-cast alloy are comprised of α -Mg, MgZnCu, Mg₂Sn, and Mg₂Zn₃ phases. During homogenization, only the MgZnCu phase remains. Complete dynamic recrystallization (DRX) takes place in the extrusion, and the spherical Mg₂Sn phase precipitates dynamically. Considerable β'_1 phase along $[0001]_{\text{Mg}}$ precipitates in the peak-aged alloy. The size of the β'_1 phase increases as the aging time is prolonged.
- 2) The mechanical properties of the peak-aged alloy are improved compared to the extruded alloy due to the strengthening effect of the β'_1 phase, with a tensile strength of 366 MPa and elongation of 7%. The mechanical properties of the over-aged alloy decrease as the strengthening effect of β'_1 is weakened. The fracture mode of the extruded and peak-

aged alloys can be a ductile-brittle mixed fracture, and the over-aged alloy is a brittle fracture mode.

- 3) The electromagnetic shielding performance of the aged alloy is improved in comparison with the extruded alloy. The growth of precipitates results in a decrease in the electromagnetic shielding property of the over-aged alloy. The peak-aged alloy exhibits the optimal electromagnetic shielding performance, with the shielding effectiveness exceeds 105 dB in the 30–1,500 MHz frequency.

DATA AVAILABILITY STATEMENT

The raw data supporting the conclusion of this article will be made available by the authors, without undue reservation.

AUTHOR CONTRIBUTIONS

YHL and MM contributed conception and design of the study. YHL organized the database and analytic results and wrote the draft of the manuscript. All authors participated in the preparation of the material. YHL and MM did the writing-review and editing.

FUNDING

This study was financially supported by The Project of Achievement Transformation of Jiangsu Province (BA2017044).

REFERENCES

Ali, Y., Qiu, D., Jiang, B., Pan, F., and Zhang, M.-X. (2015). Current Research Progress in Grain Refinement of Cast Magnesium Alloys: A Review Article. *J. Alloys Comp.* 619, 639–651. doi:10.1016/j.jallcom.2014.09.061

Alizadeh, R., Wang, J., and Llorca, J. (2021). Precipitate Strengthening of Pyramidal Slip in Mg-Zn Alloys. *Mater. Sci. Eng. A* 804, 140697. doi:10.1016/j.msea.2020.140697

Chen, X., Liu, J., and Pan, F. (2013). Enhanced Electromagnetic Interference Shielding in ZK60 Magnesium alloy by Aging Precipitation. *J. Phys. Chem. Sol.* 74, 872–878. doi:10.1016/j.jpcs.2013.02.003

- Chen, X., Liu, J., Zhang, Z., and Pan, F. (2012). Effect of Heat Treatment on Electromagnetic Shielding Effectiveness of ZK60 Magnesium alloy. *Mater. Des.* 42, 327–333. doi:10.1016/j.matdes.2012.05.061
- Chen, X., Liu, L., Liu, J., and Pan, F. (2015). Microstructure, Electromagnetic Shielding Effectiveness and Mechanical Properties of Mg-Zn-Y-Zr Alloys. *Mater. Des. (1980-2015)* 65, 360–369. doi:10.1016/j.matdes.2014.09.034
- Chen, X., Liu, L., Pan, F., Mao, J., Xu, X., and Yan, T. (2015). Microstructure, Electromagnetic Shielding Effectiveness and Mechanical Properties of Mg-Zn-Cu-Zr Alloys. *Mater. Sci. Eng. B* 197, 67–74. doi:10.1016/j.mseb.2015.03.012
- Chen, Z. H., Xia, W. J., Cheng, Y. Q., and Fu, D. F. (2005). Texture and Anisotropy in Magnesium Alloys. *Chin. J. Nonferrous Met.* 15, 1–11. doi:10.3321/j.issn:1004-0609.2005.01.001
- Cheng, L., Shuai, Z., Yu, Z., Da-Wei, Z., Chao-Zheng, H., and Zhi-Wen, L. (2014). Insights into Structural and Thermodynamic Properties of the Intermetallic Compound in Ternary Mg-Zn-Cu alloy under High Pressure and High Temperature. *J. Alloys Comp.* 597, 119–123. doi:10.1016/j.jallcom.2014.01.210
- García, A. M., Sisternas, A., and Hoyos, S. P. (2008). Occupational Exposure to Extremely Low Frequency Electric and Magnetic fields and Alzheimer Disease: a Meta-Analysis. *Int. J. Epidemiol.* 37, 329–340. doi:10.1093/ije/dym295
- Geetha, S., Sathesh Kumar, K. K., Rao, C. R. K., Vijayan, M., and Trivedi, D. C. (2009). EMI Shielding: Methods and Materials-A Review. *J. Appl. Polym. Sci.* 112, 2073–2086. doi:10.1002/app.29812
- Ghosh, P., Mezbahul-Islam, M., and Medraj, M. (2012). Critical Assessment and Thermodynamic Modeling of Mg-Zn, Mg-Sn, Sn-Zn and Mg-Sn-Zn Systems. *Calphad* 36, 28–43. doi:10.1016/j.calphad.2011.10.007
- Kabir, A. S. H., Sanjari, M., Su, J., Jung, I.-H., and Yue, S. (2014). Effect of Strain-Induced Precipitation on Dynamic Recrystallization in Mg-Al-Sn Alloys. *Mater. Sci. Eng. A* 616, 252–259. doi:10.1016/j.msea.2014.08.032
- Kim, J. T., Park, C. W., and Kim, B.-J. (2017). A Study on Synergetic EMI Shielding Behaviors of Ni-Co alloy-coated Carbon Fibers-Reinforced Composites. *Synth. Met.* 223, 212–217. doi:10.1016/j.synthmet.2016.11.027
- Kim, S.-H., and Park, S. H. (2016). Influence of Ce Addition and Homogenization Temperature on Microstructural Evolution and Mechanical Properties of Extruded Mg-Sn-Al-Zn alloy. *Mater. Sci. Eng. A* 676, 232–240. doi:10.1016/j.msea.2016.08.093
- Li, R. G., Li, H. R., Pan, H. C., Xie, D. S., Zhang, J. H., Fang, D. Q., et al. (2021). Achieving Exceptionally High Strength in Binary Mg-13Gd alloy by strong Texture and Substantial Precipitates. *Scripta Materialia* 193, 142–146. doi:10.1016/j.scriptamat.2020.10.052
- Liu, C., Chen, H., and Nie, J.-F. (2016). Interphase Boundary Segregation of Zn in Mg-Sn-Zn Alloys. *Scripta Materialia* 123, 5–8. doi:10.1016/j.scriptamat.2016.05.035
- Liu, C., Chen, X., Chen, J., Atrens, A., and Pan, F. (2020). The Effects of Ca and Mn on the Microstructure, Texture and Mechanical Properties of Mg-4 Zn alloy. *J. Magnesium Alloys* 9, 1084–1097. doi:10.1016/j.jma.2020.03.012
- Pan, H., Pan, F., Peng, J., Gou, J., Tang, A., Wu, L., et al. (2013). High-conductivity Binary Mg-Zn Sheet Processed by Cold Rolling and Subsequent Aging. *J. Alloys Comp.* 578, 493–500. doi:10.1016/j.jallcom.2013.06.082
- Pandey, R., Tekumalla, S., and Gupta, M. (2019). Enhanced (X-Band) Microwave Shielding Properties of Pure Magnesium by Addition of Diamagnetic Titanium Micro-particulates. *J. Alloys Comp.* 770, 473–482. doi:10.1016/j.jallcom.2018.08.147
- Qi, F., Zhang, D., Zhang, X., and Xu, X. X. (2014). Effect of Sn Addition on the Microstructure and Mechanical Properties of Mg-6Zn-1Mn (wt.%) alloy. *J. Alloys Compd.* 585, 656–666. doi:10.1016/j.jallcom.2013.09.156
- Rashkova, B., Prantl, W., Görgl, R., Keckes, J., Cohen, S., Bamberger, M., et al. (2008). Precipitation Processes in a Mg-Zn-Sn alloy Studied by TEM and SAXS. *Mater. Sci. Eng. A* 494, 158–165. doi:10.1016/j.msea.2008.04.005
- Ren, Y., Liu, B., Xie, H., Li, H., Jiang, M., and Qin, G. (2021). Characterization of Precipitates in Aged Mg-4 wt%Zn alloy. *Mater. Today Commun.* 26, 102017. doi:10.1016/j.mtcomm.2021.102017
- Rosalie, J. M., and Pauw, B. R. (2014). Form-free Size Distributions from Complementary Stereological TEM/SAXS on Precipitates in a Mg-Zn alloy. *Acta Materialia* 66, 150–162. doi:10.1016/j.actamat.2013.11.029
- Sasaki, T. T., Oh-ishi, K., Ohkubo, T., and Hono, K. (2011). Effect of Double Aging and Microalloying on the Age Hardening Behavior of a Mg-Sn-Zn alloy. *Mater. Sci. Eng. A* 530, 1–8. doi:10.1016/j.msea.2010.05.010
- Sasaki, T. T., Yamamoto, K., Honma, T., Kamado, S., and Hono, K. (2008). A High-Strength Mg-Sn-Zn-Al alloy Extruded at Low Temperature. *Scripta Materialia* 59, 1111–1114. doi:10.1016/j.scriptamat.2008.07.042
- Schulz, R. B., Plantz, V. C., and Brush, D. R. (1988). Shielding Theory and Practice. *IEEE Trans. Electromagn. Compat.* 30, 187–201. doi:10.1109/15.3297
- Shahzad, F., Alhabeib, M., Hatter, C. B., Anasori, B., Man Hong, S., Koo, C. M., et al. (2016). Electromagnetic Interference Shielding with 2D Transition Metal Carbides (MXenes). *Science* 353, 1137–1140. doi:10.1126/science.aag2421
- Shen, B., Zhai, W., Tao, M., Ling, J., and Zheng, W. (2013). Lightweight, Multifunctional polyetherimide/graphene@Fe3O4 Composite Foams for Shielding of Electromagnetic Pollution. *ACS Appl. Mater. Inter.* 5, 11383–11391. doi:10.1021/am4036527
- Tong, X. C. (2009). *Advanced Materials and Design for Electromagnetic Interference Shielding*. CRC Press, Taylor & Francis Group.
- Wang, C., Luo, T., Liu, Y., Huang, Q., and Yang, Y. (2021). Residual Stress and Precipitation of Mg-5Zn-3.5Sn-1Mn-0.5Ca-0.5Cu alloy with Different Quenching Rates. *J. Magnesium Alloys* 9, 604–612. doi:10.1016/j.jma.2020.02.021
- Wang, J., Wu, R., Feng, J., Zhang, J., Hou, L., and Zhang, M. (2019). Influence of Rolling Strain on Electromagnetic Shielding Property and Mechanical Properties of Dual-phase Mg-9Li alloy. *Mater. Characterization* 157, 109924. doi:10.1016/j.matchar.2019.109924
- Wang, J., Xu, L., Wu, R., Feng, J., Zhang, J., Hou, L., et al. (2020). Enhanced Electromagnetic Interference Shielding in a Duplex-phase Mg-9Li-3Al-1Zn Alloy Processed by Accumulative Roll Bonding. *Acta Metall. Sin. (Engl. Lett.)* 33, 490–499. doi:10.1007/s40195-020-01017-z
- Wang, Y., Peng, J., and Zhong, L. (2018). On the Microstructure and Mechanical Property of As-Extruded Mg-Sn-Zn alloy with Cu Addition. *J. Alloys Comp.* 744, 234–242. doi:10.1016/j.jallcom.2018.02.013
- Wei, S., Zhu, T., Hodgson, M., and Gao, W. (2013). Effects of Sn Addition on the Microstructure and Mechanical Properties of As-Cast, Rolled and Annealed Mg-4Zn Alloys. *Mater. Sci. Eng. A* 585, 139–148. doi:10.1016/j.msea.2013.07.051
- Wu, J., Jin, L., Dong, J., Wang, F., and Dong, S. (2020). The Texture and its Optimization in Magnesium alloy. *J. Mater. Sci. Tech.* 42, 175–189. doi:10.1016/j.jmst.2019.10.010
- Yang, Y., Xiong, X., Chen, J., Peng, X., Chen, D., and Pan, F. (2021). Research Advances in Magnesium and Magnesium Alloys Worldwide in 2020. *J. Magnesium Alloys* 9, 705–747. doi:10.1016/j.jma.2021.04.001
- Ye, J., Chen, X., Luo, Z., Li, J., Yuan, Y., Tan, J., et al. (2021). Improving Strength and Electromagnetic Shielding Effectiveness of Mg-Sn-Zn-Ca-Ce Alloy by Sn Addition. *Adv. Eng. Mater.* 23, 2100166. doi:10.1002/adem.202100166
- You, S., Huang, Y., Kainer, K. U., and Hort, N. (2017). Recent Research and Developments on Wrought Magnesium Alloys. *J. Magnesium Alloys* 5, 239–253. doi:10.1016/j.jma.2017.09.001
- Zhu, H. M., Sha, G., Liu, J. W., Wu, C. L., Luo, C. P., Liu, Z. W., et al. (2011). Microstructure and Mechanical Properties of Mg-6Zn-xCu-0.6Zr (wt.%) Alloys. *J. Alloys Compd.* 509, 3526–3531. doi:10.1016/j.jallcom.2010.12.165

Conflict of Interest: Authors YHL, MM, XL, YJL, GS, JY, and KZ were employed by the company GRINM Co., Ltd. Authors YHL, MM, XL, YJL, GS, JY, and KZ were employed by the company GRIMAT Engineering Institute Co., Ltd. Authors YHL, MM, XL, YJL, GS, JY, and KZ were employed by the company General Research Institute for Nonferrous Metals.

Publisher's Note: All claims expressed in this article are solely those of the authors and do not necessarily represent those of their affiliated organizations, or those of the publisher, the editors and the reviewers. Any product that may be evaluated in this article, or claim that may be made by its manufacturer, is not guaranteed or endorsed by the publisher.

Copyright © 2021 Liu, Ma, Li, Li, Shi, Yuan and Zhang. This is an open-access article distributed under the terms of the Creative Commons Attribution License (CC BY). The use, distribution or reproduction in other forums is permitted, provided the original author(s) and the copyright owner(s) are credited and that the original publication in this journal is cited, in accordance with accepted academic practice. No use, distribution or reproduction is permitted which does not comply with these terms.